Wang, Xuchen; Díaz-Rubio, Ana; Li, Huanan; Tretyakov, Sergei A.; Alù, Andrea

Theory and Design of Multifunctional Space-Time Metasurfaces

Published in:
Physical Review Applied

DOI:
10.1103/PhysRevApplied.13.044040

Published: 15/04/2020

Document Version
Publisher's PDF, also known as Version of record

Please cite the original version:
Wang, X., Díaz-Rubio, A., Li, H., Tretyakov, S. A., & Alù, A. (2020). Theory and Design of Multifunctional Space-Time Metasurfaces. *Physical Review Applied*, *13*(4), Article 044040.
https://doi.org/10.1103/PhysRevApplied.13.044040

Theory and Design of Multifunctional Space-Time Metasurfaces

Xuchen Wang,[1,*] Ana Díaz-Rubio,[1] Huanan Li,[2] Sergei A. Tretyakov,[1] and Andrea Alù[2]

[1] *Department of Electronics and Nanoengineering, Aalto University, P.O. Box 15500, FI-00076 Aalto, Finland*

[2] *Photonics Initiative, Advanced Science Research Center, City University of New York, New York, New York, USA*

(Received 12 November 2019; revised manuscript received 12 March 2020; accepted 23 March 2020; published 15 April 2020)

Integrating multiple functionalities into a single metasurface is becoming of great interest for future intelligent communication systems. While such devices have been extensively explored for reciprocal functionalities, in this work, we integrate a wide variety of nonreciprocal applications into a single platform. The proposed structure is based on spatiotemporally modulated impedance sheets supported by a grounded dielectric substrate. We show that, by engineering the excitation of evanescent modes, nonreciprocal interactions with impinging waves can be configured at will. We demonstrate a plethora of nonreciprocal components, such as wave isolators, phase shifters, and circulators, on the same metasurface. This platform allows switching between different functionalities by modifying only the pumping signals (harmonic or nonharmonic), without changing the main body of the metasurface structure. This solution opens the door for future real-time reconfigurable and environment-adaptive nonreciprocal wave controllers.

DOI: 10.1103/PhysRevApplied.13.044040

I. INTRODUCTION

The next generations of communication systems will need multifunctional devices that adapt to different usage and environment requirements, enhancing user experiences and providing better information exchange. In this emerging paradigm, because of their integration capabilities and the unprecedented opportunities for controlling waves, metasurfaces are positioned as the platform of choice to implement multifunctional responses. By varying the local properties of each composing element in space and time, one can create metasurfaces with different scattering responses. Metasurfaces can be treated as multiport devices that are able to simultaneously control waves coming in from and going out in a number of propagation directions; for example, waves coming from oppositely tilted angles [1,2]. Following the classical notation of multiport networks, the properties of a metasurface can be modeled by the scattering matrix, where each element S_{ij} represents the ratio of the flux amplitudes between the outgoing waves to port i and the incoming wave from port j. If we assume that there are no frequency transformations during scattering, the functionalities of metasurfaces can be classified into two groups: reciprocal, characterized by symmetric scattering matrices ($\overline{\overline{S}}^T = \overline{\overline{S}}$), and nonreciprocal, where the scattering matrices are asymmetric ($\overline{\overline{S}}^T \neq \overline{\overline{S}}$)

*xuchen.wang@aalto.fi

Reciprocal metasurfaces have been intensively studied in the last decade. In practice, one use *gradient* or *space-modulated* metasurfaces to tailor the scattering properties between different ports and design anomalous reflectors [3–5], beam splitters, multichannel retroreflectors [1], or asymmetric absorbers [2]. Recent advances in reciprocal metasurfaces have shown that one metasurface can perform a multitude of functionalities, switching from one application to another by reconfiguring electromagnetic parameters of the individual meta-atoms. For example, in Ref. [6], independent tunability of resistance and reactance of each unit cell using embedded tunable circuits is discussed. In this way, by local modification of the impedance of each unit cell, the metasurface can act as a perfect absorber or anomalous reflector without changing the main body of the metasurface structure.

Reciprocity imposes certain restrictions in the design of metasurfaces, and there are practical applications where it is necessary to go beyond them. Traditionally, this goal has been achieved with magneto-optical materials, such as ferrites [7] and graphene [8–10], biased by external static or slowly varying magnetic fields. But the use of bulky magnets makes these devices incompatible with integrated technologies. In addition, the weak magnetic response and high losses in the terahertz and optical ranges further inhibit their use in future optoelectronic and nanophotonic systems. One magnetless alternative is to embed nonlinear materials in resonant cavities [11–13]. By creating spatial asymmetries in the cavity, one can make the distribution of electromagnetic fields significantly different for opposite illuminations. However, this solution is restricted to strong excitation intensities, poor isolation, and nonsimultaneous excitation from different ports [14,15].

In recent years, dynamic modulation of material properties has attracted considerable attention in the physics and engineering communities due to its great potential to induce extraordinary wave phenomena [16–22]. Time-varying materials break Lorentz reciprocity in linear and magnet-free devices. Spatiotemporal modulation can impart synthetic linear or angular momentum in operating systems that emulate high-speed mechanical motion, and therefore produce Doppler-like nonreciprocity [23–25]. On the basis of this principle, many interesting phenomena have been explored [26], such as wave isolation [27–35] and circulation [36,37], one-way beam splitting [38], frequency conversion [39–41], and nonreciprocal antennas [24,42–44]. However, the nonreciprocal applications are usually fixed and unadaptable to changing environments or application requirements. While existing studies focus mostly on a specific nonreciprocal effect realized with a fixed modulation scheme, in this paper, we show that it is possible to develop robust and general means for reconfigurable nonreciprocal functionalities on a metasurface platform.

In particular, we demonstrate that by altering the space-time modulation functions it is possible to implement various canonical nonreciprocal devices on a universal platform. This multifunctional platform is based on a tunable surface-impedance sheet supported by a metallized substrate. We assume that the resistance and reactance of the surface impedance can be independently and locally controlled in real time [6]. We first develop a generalized circuit theory to characterize the scattering harmonics of surface impedances modulated with arbitrary traveling waveforms (Sec. II). The theoretical formulation allows not only direct computations of scattering harmonics for a known modulated surface impedance but also the finding of the optimal surface impedance that ensures excitation of a prescribed set of scattering harmonics. By incorporation of evanescent fields into the picture, the optimized surfaces exhibit strong and controllable nonreciprocity. On the basis of this principle, we assign optimal modulation functions to a single metasurface with fixed dimensions and demonstrate possibilities to realize isolators, phase shifters, quasi-isolators, and circulators (Sec. III). In addition, we propose viable practical implementation schemes in different frequency ranges, showing the realizability of the proposed multifunctional and adaptable platform (Sec. IV).

II. GENERALIZED CIRCUIT THEORY FOR SPACE-TIME-MODULATED SURFACES

In this section, on the basis of the surface-impedance model, we present the theoretical formulation that describes a reconfigurable platform for nonreciprocal devices. We consider the structure shown in Fig. 1(a): an electrically thin sheet mounted on a grounded substrate. The main goal is to allow arbitrary reconfiguration of the nonreciprocal functionality using spatiotemporal modulations of the electric response of the sheet.

For a general impedance sheet, its electrical properties can be defined by the parallel connection of a conductance, $G(z,t)$, and an inductance, $L(z,t)$, which are periodically modulated in space and time [see Fig. 1(a)] with spatial frequency $\beta_M = 2\pi/D$ (D is the spatial period of modulation functions) and temporal frequency $\omega_M = \beta_M = 2\pi/T$ (T is the temporal period of modulation functions). We assume that $G(z,t)$ and $B(z,t) = 1/L(z,t)$ are modulated with an arbitrary traveling waveform [the inverse of inductance, $B(z,t)$, is introduced in this paper for mathematical simplicity], and therefore they can be expressed as a sum of Fourier series [45,46]:

$$\Psi(z,t) = \sum_{m=-\infty}^{+\infty} \psi_m e^{-jm(\beta_M z - \omega_M t)}, \tag{1}$$

where Ψ denotes either G or B, and ψ_m represents g_m and b_m, which are the harmonic coefficients of $G(z,t)$ and $B(z,t)$, respectively. It is important to notice that $\psi_m^* = \psi_{-m}$ to ensure that both $G(z,t)$ and $L(z,t)$ are real-valued functions.

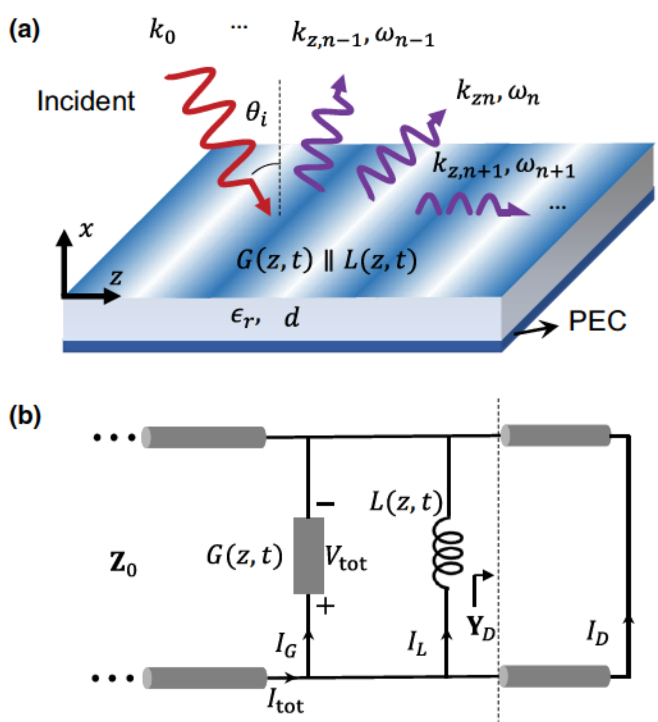

FIG. 1. (a) General scattering scenario of a space-time-modulated impenetrable surface and (b) its equivalent-circuit model. PEC, perfect electric conductor.

If a plane wave (wave number k_0 and frequency ω_0) impinges on the structure at the incidence angle $\theta = \theta_i$, according to the Floquet-Bloch theorem, the scattered fields contain an infinite number of Floquet harmonics. The nth harmonic propagates with the transverse wave number $k_{zn} = k_z + n\beta_M$ and has the frequency $\omega_n = \omega_0 + n\omega_M$ [45]. We write the tangential components of the total electrical and magnetic fields on the surface as the sum of the incident wave and all the scattered harmonics:

$$\begin{aligned} E^t_{\rm tot} &= E^t_i + E^t_s = \sum_{n=-\infty}^{+\infty} E^t_n e^{-j(k_{zn}z-\omega_n t)}, \\ H^t_{\rm tot} &= H^t_i + H^t_s = \sum_{n=-\infty}^{+\infty} H^t_n e^{-j(k_{zn}z-\omega_n t)}. \end{aligned} \tag{2}$$

The coefficients E^t_n and H^t_n can be uniquely determined by enforcing the boundary conditions on all the interfaces of the structure [see Fig. 1(a)]. However, this could be a cumbersome task, especially for structures with multiple constitutive layers. To simplify the mathematical derivations, we analyze the metasurface using the transmission-line model shown in Fig. 1(b). In this model, the spatiotemporally varying sheet is represented by a shunt impedance formed by a parallel connection of an inductor and a resistor. The metal-backed substrate is modeled as a section of transmission line with length equal to the substrate thickness. The infinitely extended transmission line at the left side of Fig. 1(b) represents free space, and its characteristic impedance, denoted as $\mathbf{Z}_0$, is the characteristic impedance of plane waves in free space. The effect of periodic modulation results in the matrix representation of all circuit components (explained in the following text). The tangential components of the total electric and magnetic fields on the surface are analogous to the total voltage $V_{\rm tot}$ and total current $I_{\rm tot}$ in the circuit ($E^t_{\rm tot} \to V_{\rm tot}$ and $H^t_{\rm tot} \to I_{\rm tot}$). From Eq. (2) we see that the voltage is composed of infinitely many harmonics:

$$V_{\rm tot}(z,t) = \sum_{n=-\infty}^{+\infty} v_n e^{-j(k_{zn}z-\omega_n t)}. \tag{3}$$

The total current is a superposition of all currents flowing in the conductance, inductance, and shorted transmission line: $I_{\rm tot} = I_G + I_L + I_D$. The partial current in each circuit component is also a sum of an infinite number of Floquet harmonics:

$$I_q(z,t) = \sum_{n=-\infty}^{+\infty} i_{q,n} e^{-j(k_{zn}z-\omega_n t)}, \quad q \in [G, L, D]. \tag{4}$$

Unlike the stationary scenario (without spatiotemporal modulation), in space-time-modulated systems, $V_{\rm tot}(z,t)$ and $I_q(z,t)$ cannot be simply related by a scalar impedance or admittance. Instead, one must consider all the harmonics from $n = -\infty$ to $n = +\infty$. Practically, we take only a finite number of harmonics from $n = -N$ to $n = +N$ into consideration (N is large enough to ensure the convergence of harmonics). The voltage and current at each element can be written as $(2N+1)$-dimensional vectors: $\vec{v} = [v_{-N}, v_{1-N}, \ldots, v_N]^T$ and $\vec{i}_q = [i_{q,-N}, i_{q,1-N}, \ldots, i_{q,N}]^T$. These voltage and current vectors can be related by a $(2N+1) \times (2N+1)$ admittance matrix $\mathbf{Y}_q$:

$$\vec{i}_q = \mathbf{Y}_q \cdot \vec{v}. \tag{5}$$

Using the linear relations between voltage and current vectors, we find the admittance matrix for each lumped component in the circuit. The current flowing in the conductance reads

$$I_G(z,t) = G(z,t) V_{\rm tot}(z,t). \tag{6}$$

After substituting Eqs. (1), (3), and (4) into Eq. (6), we have

$$\sum_{n=-\infty}^{+\infty} i_{G,n} e^{-j(k_{zn}z-\omega_n t)} = \sum_{\ell,m=-\infty}^{+\infty} g_m v_\ell e^{-j(k_{z,\ell+m}z-\omega_{\ell+m}t)}. \tag{7}$$

Using the change of variable $\ell \to \ell - m$, we can write the nth current harmonic as

$$i_{G,n} = \sum_{m=-\infty}^{+\infty} g_m v_{n-m}. \tag{8}$$

We can see that the current harmonics are not only induced by the nth voltage harmonic but are also contributed by coupling with other harmonics. Equation (8) must be satisfied for all harmonics, generating a system of equations formed by $2N+1$ linear equations ($n \in [-N, N]$). The equations can be written in the matrix form $\vec{i}_G = \mathbf{Y}_G \cdot \vec{v}$, which can be expanded as

$$\begin{pmatrix} i_{G,-N} \\ i_{G,1-N} \\ \vdots \\ i_{G,N} \end{pmatrix} = \begin{pmatrix} g_0 & g_{-1} & \cdots & g_{-2N} \\ g_1 & g_0 & \cdots & g_{1-2N} \\ \vdots & \vdots & \ddots & \vdots \\ g_{2N} & g_{2N-1} & \cdots & g_0 \end{pmatrix} \begin{pmatrix} v_{-N} \\ v_{1-N} \\ \vdots \\ v_N \end{pmatrix}. \tag{9}$$

Here $\mathbf{Y}_G$ is called the "admittance matrix." $\mathbf{Y}_G$ is a Toeplitz matrix with elements $Y_G(s,t) = g_{s-t}$, where $s, t \in [-N, N]$ are the row and column indexes of the matrix, respectively.

Following a similar approach, we derive the admittance matrix for the space-time-modulated inductance. The time-domain relation between the current and voltage across a time-varying inductor reads

$$I_L(z,t)L(z,t) = \int^t V_{\text{tot}}(z,t')dt'. \tag{10}$$

After substituting Eqs. (1) and (4) into Eq. (10) and using the same mathematical treatments in Eq. (7), we can find the admittance matrix of inductance, $\mathbf{Y}_L$ which is filled by matrix element $Y_L(s,t) = b_{s-t}/j\omega_t$ [45].

Finally, we need to calculate the admittance matrix of the shorted transmission line, $\mathbf{Y}_D$. Different Floquet modes have different frequencies and propagation constants in the substrate. Since the substrate is not modulated, there are no coupling elements in $\mathbf{Y}_D$. Therefore, $\mathbf{Y}_D$ is a diagonal matrix with elements $Y_D(n,n) = y_{D,n}$, where $y_{D,n}$ is the input admittance of the shorted transmission line for the nth harmonic. Following the derivation in Sec. 2.7 in Ref. [47], we can obtain the expression for $y_{D,n}$ [45]:

$$y_{D,n} = \frac{1}{z_{D,n}^{\text{TM}} \tanh jk_{xn}^D d}, \tag{11}$$

where $k_{xn}^D = \sqrt{\omega_n^2 \epsilon_r \epsilon_0 \mu_0 - k_{zn}^2}$ is the normal component of the wave number in the dielectric substrate and $z_{D,n}^{\text{TM}} = k_{xn}^D/\epsilon_r \epsilon_0 \omega_n$ is the TM-wave impedance of the dielectric substrate.

After the admittance matrices for all the circuit components are determined, the total admittance is defined as $\mathbf{Y}_{\text{tot}} = \mathbf{Y}_G + \mathbf{Y}_L + \mathbf{Y}_D$. This matrix relates the total current and voltage (summation of the incident and reflected harmonics) of the circuit:

$$\vec{i}^{\text{in}} - \vec{i}^{\text{re}} = \mathbf{Y}_{\text{tot}} \cdot (\vec{v}^{\text{in}} + \vec{v}^{\text{re}}), \tag{12}$$

where the superscripts "in" and "re" represent the incident and reflected harmonics, respectively. The tangential electrical and magnetic fields of the incident and scattered harmonics are related by the characteristic impedance matrix of free space $\mathbf{Z}_0$. For TM incidence, the impedance $\mathbf{Z}_0$ is a diagonal matrix filled with $Z_0(n,n) = z_{0,n}^{\text{TM}} = k_{xn}^0/\epsilon_0\omega_n$, where $k_{xn}^0 = \sqrt{\omega_n^2 \epsilon_0 \mu_0 - k_{zn}^2}$ is the vertical wave vector of the nth harmonic. Therefore, we have

$$\vec{v}^{\text{in}} = \mathbf{Z}_0 \cdot \vec{i}^{\text{in}}, \quad \vec{v}^{\text{re}} = \mathbf{Z}_0 \cdot \vec{i}^{\text{re}}. \tag{13}$$

Substituting Eq. (13) into Eq. (12), we can find $\vec{i}^{\text{re}} = -\mathbf{\Gamma} \cdot \vec{i}^{\text{in}}$. The parameter $\mathbf{\Gamma}$ is called the "reflection matrix" and is given by

$$\mathbf{\Gamma} = (\mathbf{Y}_{\text{tot}}\mathbf{Z}_0 + \mathbf{I})^{-1}(\mathbf{Y}_{\text{tot}}\mathbf{Z}_0 - \mathbf{I}), \tag{14}$$

where $\mathbf{I}$ is the $(2N+1) \times (2N+1)$ unity matrix. The source vector is defined as $\vec{i}^{\text{in}} = [0,\ldots,0,1,0,\ldots,0]^T$. We can see that the nth reflected harmonic is equal to the matrix element located in the nth row and zeroth column of the reflection matrix $\mathbf{\Gamma}$, $i_n^{\text{re}} = \Gamma(n,0)$.

If the surface conductance and inductance in Fig. 1(b) and the substrate properties are known, for a specific plane-wave excitation the scattering harmonics are uniquely determined by Eq. (14). Alternatively, for desired scattering responses, it is also possible to find properly modulated conductance and inductance that correspond to the generation of the desired scattering harmonics by the metasurface. However, there is no simple analytical formulation that can directly determine the modulation functions for a set of desired scattering harmonics. For this reason, we mathematically optimize the Fourier coefficients of the modulation functions $G(z,t)$ and $B(z,t)$ until they generate the desired harmonics for two opposite incident directions ($\theta = +\theta_i$ and $\theta = -\theta_i$), realizing desired nonreciprocal effects.

III. ENGINEERING NONRECIPROCITY OF SPACE-TIME-MODULATED METASURFACES

In this section, we show that the generalized circuit model developed in Sec. II can be used to realize different nonreciprocal devices engineering modulation functions. As examples, we design isolators, nonreciprocal phase shifters, quasi-isolators, and circulators on a physically rigid platform by modifying only the modulation functions.

A. Metasurface isolators

An isolator is a lossy, passive, and matched two-port device that allows unidirectional wave transmission [47]. For a perfect isolator, waves incident on one port are fully dissipated, while the waves incident on the second port are fully transmitted without frequency conversion. The scattering matrix of an ideal isolator is defined as

$$\overline{\overline{S}} = \begin{pmatrix} 0 & 1 \\ 0 & 0 \end{pmatrix}. \tag{15}$$

Figure 2 shows the design principle of the metasurface isolator. Plane waves incident at $\theta = +\theta_i$ (port 1) are completely absorbed, while waves incident at $\theta = -\theta_i$ (port 2) are all specularly reflected into port 1 ($n = 0$). It is important to note that, according to this definition, there is no frequency conversion between ports.

Wave isolation realized with space-time-modulated media has been demonstrated in a few papers [30,32,36,48],

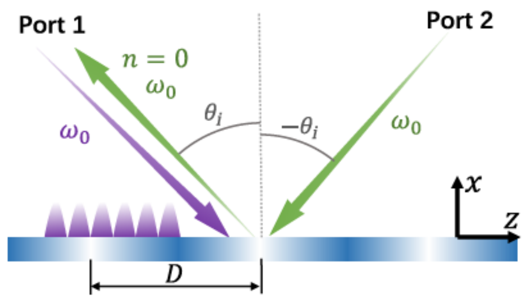

FIG. 2. The metasurface platform for implementing isolators.

where the classical scattering matrix [see Eq. (15)] is not suitable to describe those systems. In those studies, the incident wave from the attenuation port was not absorbed due to material losses but was converted to higher-order harmonics and transmitted, requiring absorptive filters to remove the generated harmonics. In other work [35], although there was no frequency conversion of the scattered propagating waves, the waves incident from the attenuation port were not actually absorbed but leaked away through other ports (transmission side). Here we propose a solution based on a lossy gradient surface impedance that allows us to design isolators according to the classical definition shown in Eq. (15). The design method consists of three steps:

(a) Step 1. With use of the multichannel metasurface concept, the first step in the design is to find the period of the metasurface space modulation that allows the required propagating channels. In this case, the two-port system is implemented in the metasurface platform by the incident direction and the specular reflection, as shown in Fig. 2. This condition can be fulfilled by restricting the spatial period as $D < \lambda_0/(1 + \sin\theta_i)$ [45]. In addition, this periodicity ensures that both S_{11} and S_{22} are zero (no retroreflection or other higher-order diffraction modes).

(b) Step 2. Once the spatial period of the metasurface has been chosen, the second step is to find a proper traveling-wave modulation profile that can realize perfect absorption for a plane wave incident from $\theta = +\theta_i$ (port 1). We define the frequency of incidence as $\omega_0 = \omega_d$, and the modulation frequency is $\omega_M = \omega_d/10^3$. For total absorption at port 1, the scattered field should have no specular reflection, which means

$$|\Gamma(0, 0)| = 0 \tag{16}$$

should be satisfied for incidence of $\theta = +\theta_i$. Next, we ensure strong *evanescent fields* are excited simultaneously, which is the key point of this design method. The reason for the excitation of evanescent fields is because the wavelength of these fields is much smaller than the spatial modulation periodicity, and they are generated to locally satisfy the gradient impedance boundary condition. Therefore, they tend to be sensitive to the surface boundary perturbation, as well as the incident angles. Furthermore, the amplitudes of evanescent fields can control the resonance strength. To guarantee the excitation of evanescent fields, we impose

$$|\Gamma(1, 0)| = A_1. \tag{17}$$

Notice that we only need to ensure the desired amplitude of the first-order evanescent mode ($n = 1$). Equations (16) and (17) are called "objective functions" that guarantee evanescent-field-induced absorption at port 1.

Next we aim to find the optimal surface impedance that can satisfy these two objectives. From the results in Sec. II we know that $\Gamma(n, 0)$ are determined by the Fourier coefficients of $G(z, t)$ and $B(z, t)$. To find g_m and b_m that satisfy the objectives, we can introduce unlimited numbers of g_m and b_m in Eq. (1). However, we assume that only three Fourier terms are enough to adequately describe each component [$g_{0,\pm1}$ for $G(z, t)$ and $b_{0,\pm1}$ for $B(z, t)$]. Without loss of generality, we also assume that $g_m = g_{-m}$ and $b_m = b_{-m}$ (this assumption always holds in the following text), such that the Fourier terms are real numbers and both $G(z, t)$ and $B(z, t)$ are even functions with respect to the z axis. Under these assumptions, the Fourier series for $G(z, t)$ and $B(z, t)$ in Eq. (1) are reduced to

$$G(z, t) = g_0 + 2g_1 \cos(\beta_M z - \omega_M t) \tag{18}$$

and

$$B(z, t) = b_0 + 2b_1 \cos(\beta_M z - \omega_M t). \tag{19}$$

At this point, to preserve the physical meaning of the model, one must ensure that the conductance and inductance are always positive along the z axis. To do that, two additional constraints are introduced, $g_0 - 2|g_1| > 0$ and $b_0 - 2|b_1| > 0$.

In total, there are two objective equations and two linear constraints to be considered with four unknown Fourier coefficients. To solve this optimization problem, we use MATLAB OPTIMIZATION TOOLBOX to find the solutions of Eqs. (16) and (17), using the optimization function fmincon (optimization code is available in Ref. [45]). Table I shows the optimized b_m and g_m for different evanescent-field amplitudes.

(c) Step 3. Once the surface impedance satisfying the objective functions at $\theta = +\theta_i$ has been optimized, we examine its scattering fields for $\theta = -\theta_i$ using the mode-matching method presented in Sec. II.

For incidence from port 2, the resonance shifts to higher frequency (dashed line in Fig. 3). The space-time-modulated surface emulates a moving slab with velocity $v_M = \omega_M/\beta_M$ along the $+z$ direction. Effective motion of

TABLE I. Optimized amplitudes of the Fourier harmonics for different values of the desired evanescent-field amplitude. We assume $D = 0.419\lambda_d$ ($\lambda_d = 2\pi c/\omega_d$, where c is the speed of light). The substrate has relative permittivity $\epsilon_r = 4$ and thickness $d = 0.133\lambda_d$ (the same substrate is used throughout Sec. III).

Evanescent field ($n = 1$)	$g_0 \times 10^{-6}$	$g_1 \times 10^{-6}$	$b_0 \times 10^{10}$	$b_1 \times 10^{10}$	$\|S_{12}\|^2$ (dB)	$\|S_{21}\|^2$ (dB)
$A_1 = 1$	208.15	−38.1	43.36	−11.42	−21.6	−83
$A_1 = 3$	26.17	−5.50	36.03	−3.46	−5.37	−64
$A_1 = 10$	2.29	−0.67	35.25	−1.03	−0.08	−43.7

the metasurface compromises the established phase matching of the incident plane wave and one of the surface modes (as deigned in step 2). For incidence from port 2, the phase-matching condition holds at lower frequencies. This effect is similar to the phenomenon in Ref. [35], based on asymmetric distortion of the dispersion diagram under traveling-wave modulation. For the case of $A_1 = 1$, although nonreciprocity is achieved, the isolation performance at the defined frequency $\omega_0 = \omega_d$ is not good, since the wave incident from port 2 is almost absorbed ($|S_{12}|^2 < -20$ dB). To obtain near-perfect isolation, the amplitude of the evanescent field A_1 should be further increased. We see that as A_1 increases, the resonance become stronger. When $A_1 = 10$ (yellow curves), near-perfect isolation is achieved at $\omega_0 = \omega_d$. In this case, the wave incident from port 1 is completely absorbed, while the wave from port 2 it is fully delivered to port 1 (the efficiencies of both absorption and transmission are above 99%). The above design procedures are summarized in Fig. 4: We first optimize the modulation functions that ensure the desired propagation modes as well as the evanescent modes for the forward direction (steps A–C). Then we examine the scattered harmonics for the backward direction and check the achieved level of nonreciprocity (step D). If the nonreciprocity is not strong, we further enhance the amplitude of the evanescent mode

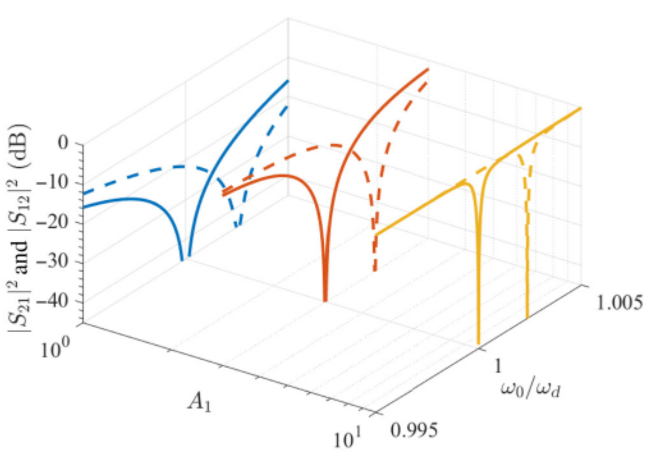

FIG. 3. Transmittances for incidences from port 1 (S_{21}: solid lines) and port 2 (S_{12}: dashed lines). $S_{21} = \Gamma(0, 0)$ for incidence from port 1 and $S_{12} = \Gamma(0, 0)$ for incidence from port 2. In the three scenarios, the designed amplitudes of the $n = 1$ evanescent mode are $A_1 = 1$ (blue), $A_1 = 3$ (red), and $A_1 = 10$ (yellow).

A_1 defined in step B and optimize the modulation function until it satisfies the desired nonreciprocal functionality. In the next subsections, on the basis of this design procedure, we realize and engineer other nonreciprocal functionalities on the same physical platform.

B. Metasurface nonreciprocal phase shifters

In lossless nonreciprocal phase shifters, the phase shifts for waves traveling between their two ports in opposite directions differ by a specific phase difference $\Delta\varphi$. The scattering matrix of a lossless and matched phase shifter can be generally represented as

$$\overline{\overline{S}} = \begin{pmatrix} 0 & e^{j(\varphi_1+\Delta\varphi)} \\ e^{j\varphi_1} & 0 \end{pmatrix}. \tag{20}$$

A schematic of the proposed nonreciprocal metasurface phase shifter is shown in Fig. 5. Light incident from $\theta = +\theta_i$ (port 1) is fully reflected (i.e., transmitted into port 2) with transmission phase φ_1, while from the opposite direction $\theta = -\theta_i$ (port 2), the transmission phase is $\varphi_2 = \varphi_1 + \Delta\varphi$.

As far as we know, space-time metasurfaces providing nonreciprocal phase shifts for free-space propagation have not yet been reported. Here we demonstrate that by engineering induced evanescent fields it is possible to create metasurface phase shifters with controllable differential phases. The proposed design method consists of the following steps:

(a) Step 1. Similarly to the design of metasurface isolators, the period of the metasurface phase shifter is selected within the range $D < \lambda_0/(1 + \sin\theta_i)$ to allow only

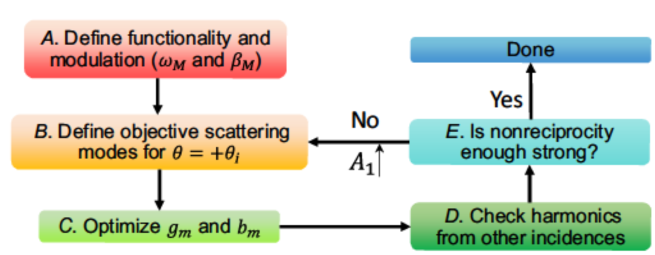

FIG. 4. Block diagram of the design procedure for all exemplary devices proposed in Sec. III.

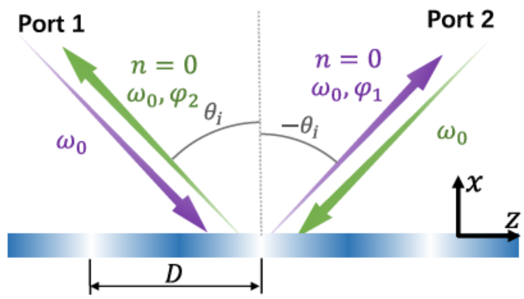

FIG. 5. Metasurface phase shifter for arbitrary phase conversion between two ports.

specular reflection. This condition will guarantee $S_{11} = S_{22} = 0$.

(b) Step 2. Next we ensure proper excitation of resonant evanescent fields for incidence of $\theta = +\theta_i$. As we know from the design principle of the metasurface isolator (Sec. III A), such resonance is very sensitive to the transverse unidirectional modulation momentum, and the resonance frequency is expected to shift at the opposite incidence ($\theta = -\theta_i$). Following this idea, we introduce one objective function $|\Gamma(1,0)| = A_1$ at $\theta = +\theta_i$, which guarantees that the first-order evanescent field is excited with amplitude A_1. Since the system is required to be lossless, the surface conductance is removed ($G = 0$), and only the inductance is subject to modulation. We assume a simple harmonic modulation waveform on $B(z,t)$:

$$B(z,t) = b_0 + 2b_1 \cos(\beta_M z - \omega_M t), \qquad (21)$$

where $\omega_M = 0.01\omega_d$. Notice that the constraint $b_0 - 2|b_1| > 0$ should be imposed to guarantee that the inductance values remain positive. Using optimization, we can find a proper set of b_0 and b_1 to ensure that $A_1 = 3$ (as an example). We can see from Fig. 6 (solid blue line) that

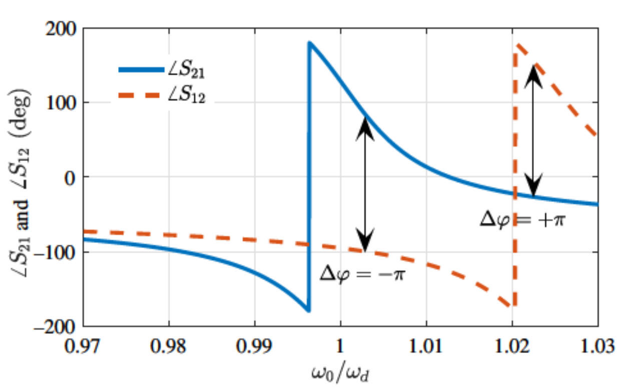

FIG. 6. Transmission phases for waves incident at $\theta = +45°$ (port 1) and $\theta = -45°$ (port 2). The surface impedance studied is synthesized with $b_0 = 39.85 \times 10^{10}$ and $b_1 = -7.50 \times 10^{10}$. The spatial period $D = 0.419\lambda_d$.

the transmission phase has an abrupt change around the defined resonant frequency ω_d.

(c) Step 3. After obtaining the optimal surface impedance, we investigate its transmission phase for the opposite incidence. Similarly to the case of metasurface isolators (see Sec. III A), sharp resonance in the phase spectrum shifts to higher frequency, creating a large phase difference at a fixed frequency. For example, at $\omega_0 = 1.003\omega_d$ and $\omega_0 = 1.023\omega_d$, the devices exhibits $-\pi$ and $+\pi$ phase shifts for waves traveling in the opposite directions, which can be practically used as a gyrator. The phase shift is continuously tunable by increasing or decreasing the modulation frequency, which adjusts the spectral distances of the two resonances. The frequency bandwidth of such phase shifters depends on the quality factor of the resonance, which is determined by A_1. Decreasing A_1 and increasing the modulation frequency, we can obtain a flatter phase curve, which effectively expands the frequency bandwidth.

C. Metasurface quasi-isolators

In Sec. III A, we showed how one can realize wave isolators using lossy modulated impedance sheets and demonstrated near-perfect isolation without the need for frequency filters. Here we show that wave isolation can be realized also in lossless two-port systems, as schematized in Fig. 7. Instead of being absorbed, as in usual isolators, the energy from port 1 is fully reflected back (retroreflection) with frequency conversion $\omega_0 \to \omega_0 - \omega_M$, while the energy from port 2 is fully delivered to port 1 (specular reflection) without frequency conversion ($\omega_0 \to \omega_0$). It is important to note that although frequency conversion occurs when the system is illuminated from port 1, this higher-order harmonic is not delivered to port 2 and, for this reason, frequency filters are still not necessary. These devices provide the same functionality as ideal isolators if one considers the signal frequency, and therefore we call them "quasi-isolators." Ideal lossless isolators without frequency conversion or conversion to some other mode or channel are forbidden by energy conservation. The design of these devices has two steps:

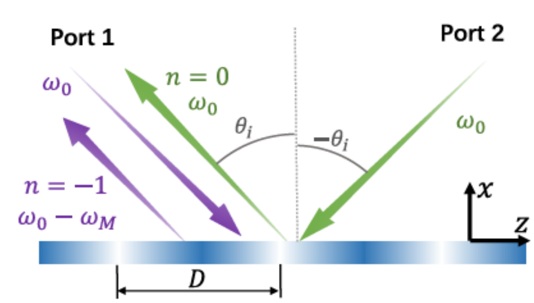

FIG. 7. A quasi-isolator implemented in the proposed metasurface platform.

TABLE II. Optimized amplitudes of the Fourier harmonics for different values of the evanescent-field amplitude.

Evanescent field ($n = 1$)	$b_0 \times 10^{10}$	$b_1 \times 10^{10}$	$b_2 \times 10^{10}$	$\lvert S_{12}\rvert^2$ (dB)	$\lvert S_{21}\rvert^2$ (dB)
$A_1 = 1$	229.83	30.19	−37.70	−15.73	−81.87
$A_1 = 3$	192.52	12.34	−13.86	−2.41	−46.02
$A_1 = 10$	187.79	−6.30	6.13	−0.04	−42.42

(a) Step 1. The first step is to define the spatial period of the metasurface that allows not only specular reflection but also retroreflection. This requirement can be satisfied by choosing $D = \lambda_0/2\sin\theta_i$. In this case, we still create a two-port system, but the incident waves are allowed to reflect back into the same port (retroreflection). Notice that the difference from the lossy isolator, where the condition $S_{11} = S_{22} = 0$ was automatically fulfilled by choosing the period that does not allow propagation of any diffracted mode, including the retroreflected one.

(b) Step 2. The second step is to realize perfect retroreflection for incidence from port 1 ($\theta = +\theta_i$) at the target frequency ω_d. In the case of ideal retroreflection the energy transmitted to port 2 is zero due to energy conservation. In addition, the evanescent fields should be specified to control the Q factor of the system. Taking these factors into consideration, we define two objectives for incidence from $\theta = +\theta_i$:

$$|\Gamma(-1,0)| = 1, \quad |\Gamma(1,0)| = A_1. \tag{22}$$

Combining these objectives with the linear condition that guarantees only positive values of the inductance, $B(z,t) > 0$, one can see that at least 3 degrees of freedom are required to specify the system. For this reason, three unknowns (b_0, b_1, and b_2) are introduced to synthesize $B(z,t)$. We can write the expression for $B(z,t)$ as

$$B(z,t) = b_0 + \sum_{m=1}^{m=2} 2b_m \cos[m(\beta_M z - \omega_M t)], \tag{23}$$

where modulation frequency $\omega_M = 2\omega_d/10^4$ is assumed in this example. Using optimization tools, we find the Fourier coefficients for three different values of A_1, shown in Table II.

Figure 8 presents the scattered harmonics at two opposite incidence angles for two optimal surfaces. The first panel shows the results for $A_1 = 1$. We can see that the harmonics excited by plane waves at ports 1 and 2 (incidence angles $+45^\circ$ and -45°) are almost identical, meaning that if the amplitude of the first-order evanescent harmonic is so small, there is no significant phase mismatch for excitation from the other port. Therefore, waves incident on both ports are reflected back into the same port. However, as A_1 increases, the enhanced resonance of evanescent fields becomes more sensitive to the angle of illumination. For the case when $A_1 = 10$, the excited evanescent modes are completely different for illuminations from the opposite angles, which leads to enhanced transmission from port 2 to port 1 and realization of the quasi-isolator regime. These results again show that we can impose strong evanescent fields (increase Q factor) to achieve evident efficiency of the nonreciprocal devices.

D. Metasurface circulators

With the proper choice of the spatial period and use of a more-complex time-modulation function, it is possible to control nonreciprocal wave propagation between more ports. As a particular example, we use the design method explained above to realize three-port metasurface circulators. Figure 9 shows the schematics of the proposed metasurface circulator, where the incident wave travels unidirectionally between three ports: $1 \to 3$, $3 \to 2$, and $2 \to 1$. It is important to note that the device introduces frequency down-conversion ($\omega_0 \to \omega_0 - \omega_M$) for propagation from port 1 to port 3, and up-conversion ($\omega_0 - \omega_M \to \omega_0$) for propagation from port 3 to port 2. A similar functionality was realized in recent work [36] exciting two independent optical modes with transition momentum (β_M, ω_M) in the dispersion diagrams and creating a

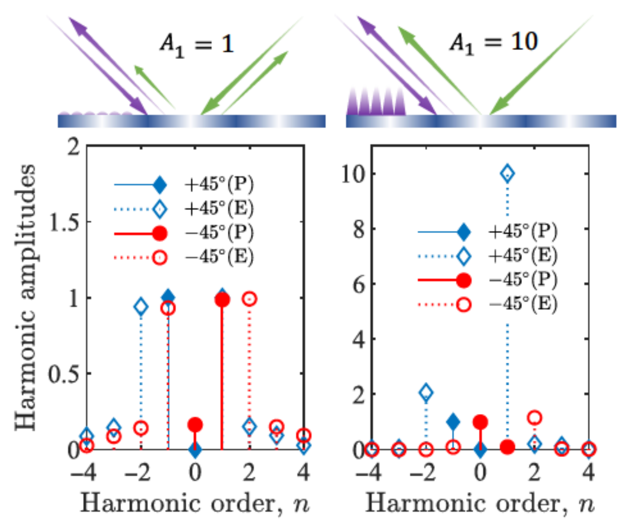

FIG. 8. The amplitudes of excited harmonics for incidences from $+45^\circ$ and -45° at $\omega_0 = \omega_d$. From left to right, the amplitudes of evanescent mode $n = +1$ are $A_1 = 1$, and $A_1 = 10$, respectively. E, evanescent modes; P, propagating modes.

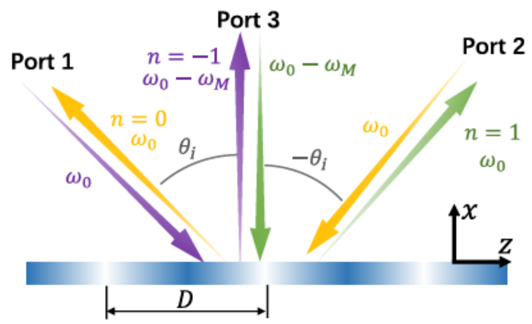

FIG. 9. A metasurface circulator.

high-quality resonator system. However, the known design method needs careful numerical optimizations of the band structures to ensure proper support of multiple optical modes. In addition, these optical modes should be tailored to be strongly resonant (high Q) to spectrally resolve them.

Here we show that using the mode-matching method and mathematical optimization, one can easily find surface impedances that realize perfect wave circulation, thus avoiding complicated band-structure engineering. The design method for metasurface circulators consists of two steps:

(a) Step 1. First we increase the spatial period of the metasurface to $D=\lambda_0/\sin\theta_i$. This periodicity allows propagation of two additional diffracted modes for an incidence angle of $\theta=\theta_i$ (wave from port 1 can be retroreflected or delivered to port 3), so the metasurface can be viewed as a three-port system (see Fig. 9).

(b) Step 2. The second step is to find the modulation functions for the metasurface-circulator design. Enforcing the requirement that waves incident from port 1 are fully directed to port 3 and considering that the system is space-time modulated ($\omega_M\neq 0$), we find that the amplitude of the $n=-1$ diffraction mode should be $|\Gamma(-1,0)|=1/\cos\theta_i$ due to the energy-conservation principle [4]. This condition automatically ensures photonic transition between two different optical modes as Ref. [36] aims to achieve. Then we prescribe the amplitude of the first-order evanescent-field harmonic as $|\Gamma(1,0)|=A_1$ to control the quality factor of the system.

In the system optimization we define two objectives corresponding to the above requirements for harmonics. However, as the number of ports increases, the positive-inductance condition is more difficult to satisfy if we introduce only a few Fourier terms in the modulation function. For this reason, more Fourier harmonics are included in $B(z,t)$ to provide more freedom in the construction of a purely inductive modulated sheet impedance. In particular, we introduce five unknowns in $B(z,t)$:

$$B(z,t)=b_0+\sum_{m=1}^{m=4}2b_m\cos[m(\beta_M z-\omega_M t)]. \tag{24}$$

Next the Fourier harmonics of $B(z,t)$ are optimized; the resulting values for the harmonics are summarized in the caption for Fig. 10.

We now examine the scattering harmonics when the circulator is illuminated from each of the three ports. The results are shown in Fig. 10. In the first scenario (left panel in Fig. 10), the wave incident from $\theta=+\theta_i$ is fully delivered to the normal direction (port 3) with strong evanescent fields excited on the surface. In the second scenario (middle panel in Fig. 10), the wave incident from port 3 goes to port 2 and excites the same sets of evanescent fields as in scenario 1. This behavior is ensured by the phase-matching condition established for scenario 1.

Finally, for the wave incident from $\theta=-\theta_i$ (port 3), the incident wave propagates in the direction opposite that of

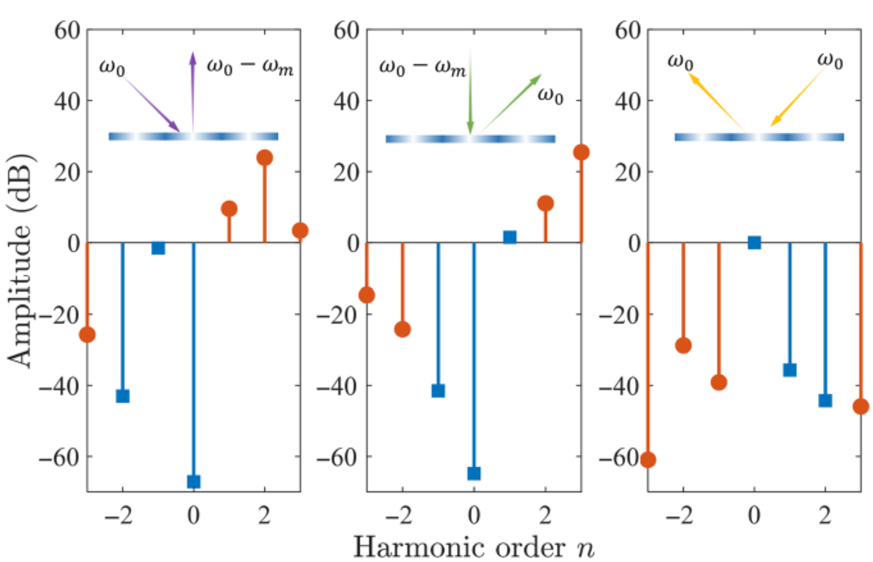

FIG. 10. Calculated harmonics for excitation from $\theta=+45^\circ$ (left), $\theta=0^\circ$ (middle), and $\theta=-45^\circ$ (right). The modulation frequency $\omega_M=\omega_d/10^3$. The blue squares represents propagating modes and the orange circles represent evanescent modes. The optimized harmonic amplitudes of $B(z,t)$ are $b_0=198.54\times 10^{10}$, $b_1=22.71\times 10^{10}$, $b_2=8.77\times 10^{10}$, $b_3=7.18\times 10^{10}$, and $b_4=1.47\times 10^{10}$. The prescribed evanescent-field amplitude is $A_1=3$.

the modulation wave. Because of the strong phase mismatch, the resonance disappears and the device behaves as a normal mirror with full transmission to port 1.

As the number of channels increases, more Fourier harmonics should be incorporated in the design of the modulation function, which opens up the possibility to realize wave circulation between five or more ports.

IV. POSSIBLE IMPLEMENTATIONS IN MICROWAVE AND TERAHERTZ RANGES

In Sec. III we demonstrated that various nonreciprocal functionalities can be realized within the proposed space-time-modulated surface-impedance platform. Surface impedance is one of the most commonly used models for the design of metasurfaces; see, for example, Sec. 2.4.3 in Ref. [49]. The required surface impedance can be implemented by structuring a metallic layer into periodic patterns [2,50]. Dynamical modulation of surface impedance can be realized by embedding tunable elements or materials in meta-atoms (unit cells of the metasurface); see, for example, [51]. In the microwave and millimeter-wave bands, surface impedance of meta-atom arrays can be controlled by varactors and varistors. This method was experimentally demonstrated in the design of tunable reciprocal metasurfaces [52–54], as well as nonreciprocal space-time devices by modulating varactors in a traveling-wave form [24,33,44]. In the terahertz range, tunable lumped components are not practical to use due to the reduced footprint. Graphene, a two-dimensional material with gate-controlled surface impedance, can be used for realization of spatiotemporal surface impedances due to its gate-controlled sheet impedance. In this section, we discuss implementation possibilities of the proposed multifunctional platform, based on tunable lumped components in the microwave band and graphene in the terahertz band.

A. Implementation based on reconfigurable intelligent surfaces

With modern integrated-circuit technology, both varactors and varistors can be packaged inside a single chip and their values can be independently controlled by external signals [55]. The control chip is then connected to each meta-atom to dynamically modify the local surface resistance and reactance of metasurfaces. A schematic of a suitable hardware platform was proposed in Refs. [56,57]. Meta-atoms are formed by four patches, and each of them is pinned to the other side of metasurfaces and connected to controller chips (see Fig.1 in Ref. [56]). The ground plane is positioned between the patch layer and the chip layer, which reduces interactions between electromagnetic waves and control circuitry. The chips are connected to each other by signal lines. With proper instructions from the computer, the meta-atoms are properly modulated [58] to control the effective surface impedance of each element. Such a modulation platform has been used to achieve reconfigurability of reciprocal metasurfaces [6], where the electrical properties of the surface are modulated in space. By applying a time-varying control signal on each chip, the surface impedance of the metasurface can be spatiotemporally modulated and the modulation function can change in time to provide multiple nonreciprocal functionalities as required.

It is worth mentioning that in the theoretical model presented here we assume the modulation of inductance, but in practical implementation it is usually easier to realize temporal modulation of capacitance than inductance. The design equations for capacitive reactance can be derived in the same way as shown above for inductive sheets. Alternatively, it may be reasonable to mimic time-varying inductance using a large fixed inductance in series with a time-modulated capacitance of the control chip. In this way, the total reactance is inductive and modulated in time, producing the same effect as a time-varying inductance.

B. Implementations based on a graphene platform

In the terahertz and mid-infrared band, graphene is a good candidate to implement the tunable component of space-time-modulated metasurfaces due to its tunable electrical conductivity and compatibility with advanced nanofabrication technologies [30,31,39,40,43]. Considering that graphene is a lossy material, in this section we show how one can use space-time-modulated graphene sheets to create tunable wave isolators in the terahertz range.

The sheet conductivity of graphene can be effectively modified via electrical bias or optical pumping. This provides the possibility of synthesizing space-time-modulated surface impedances by locally varying the bias voltage applied on graphene. The sheet conductivity of graphene in the low terahertz range can be modeled as

$$\sigma_s = \frac{\sigma_0}{1 + j\omega\tau}, \tag{25}$$

where

$$\sigma_0 = \frac{e^2 \tau k_B T}{\pi \hbar^2}\left[\frac{E_{F0}}{k_B T} + 2\ln\left(e^{-E_{F0}/k_B T} + 1\right)\right] \tag{26}$$

is the dc conductivity, τ is the electron scattering time, e is the electron charge, and E_{F0} is the Fermi level of graphene, which can be controlled by the external voltage. As can be seen from Eqs. (25) and (26), graphene is naturally resistive and inductive in the terahertz range, and its sheet impedance can be expressed as $Z_g = 1/\sigma_s = R_s + jX_s$. If a spatiotemporally varying gate voltage is applied on a graphene strip, both its sheet resistance ($R_s = 1/\sigma_0$) and its inductance ($L_s = \tau/\sigma_0$) can be harmonically modulated with the same pumping scheme.

Figure 11 shows a schematic representation of the proposed design where graphene strips are periodically positioned on top of a metallized substrate. For the convenience of gating, a pair of graphene strips are separated by a thin dielectric film (e.g., Al_2O_3) to form a self-capacitor [30]. Because of the stacked structure, the effective sheet impedance of graphene is reduced to half of the impedance of single-layer graphene. Under TM-polarized incidence, the electrical response of graphene patterns can be described as a series of resistance, inductance, and capacitance (all of them are effective values). The static resistance and inductance of graphene without modulation are

$$R_0 = \frac{R_s}{2}\left(\frac{P-g}{g}\right), \quad L_0 = \frac{L_s}{2}\left(\frac{P-g}{g}\right), \tag{27}$$

where P is the period of the graphene-strip array, g is the distance between two adjacent graphene strips, and $(P-g)/g$ is the structural factor that takes into account the increase of resistance and inductance due to the patterning of graphene [50]. The capacitance C_0 is contributed by capacitive coupling of the adjacent strips [59]:

$$C_0 = \frac{2}{\pi}\epsilon_{\text{eff}}\epsilon_0 P \ln\left[\left(\frac{\pi g}{2P}\right)\right], \tag{28}$$

with effective permittivity $\epsilon_{\text{eff}} = (\epsilon_r + 1)/2$. Equation (28) becomes invalid for very thin substrates ($d < 0.3P$),

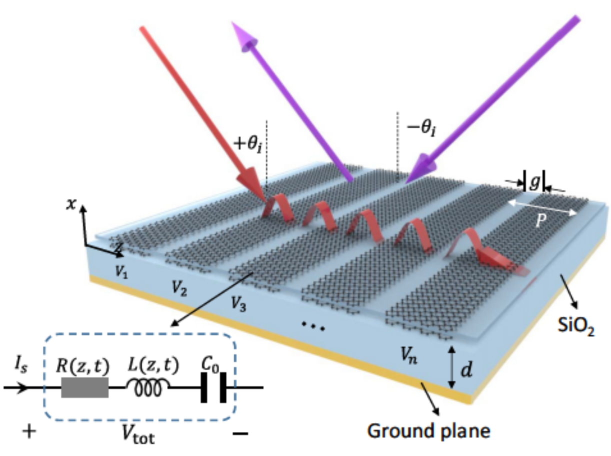

FIG. 11. A practical design. The surface impedance of one unit cell is implemented by periodically arranged graphene strips (subcells). The size P of one subcell is 2 μm, and the gap g between two neighboring strips 100 nm. The permittivity ϵ_r of the SiO_2 substrate is 4, and its thickness d is 4 μm. The local gate voltages on graphene are changing with time. When a wave is incident from $\theta = +\theta_i$, it is transformed into evanescent fields and eventually dissipated in graphene (red wave). For incidence at $\theta = -\theta_i$, it is reflected in the specular direction (purple wave).

because in this case the near-field coupling between graphene strips and the ground plane should also be considered [60]. In the present design ($d > 0.3P$), Eq. (28) is valid and the capacitance is determined only by the structuring of graphene and the substrate permittivity; therefore, it does not change during the modulation. A pump voltage is applied on graphene, and the resistance and inductance of graphene are modulated around their static values. We assume a modulation function in the form

$$f_M(z,t) = a_0 + \sum_{m=1}^{+\infty} 2a_m \cos[m(\beta_M z - \omega_M t)], \tag{29}$$

with $a_0 = 1$. Thus, the space-time lumped values are $R(z,t) = R_0 f_M(z,t)$ and $L(z,t) = L_0 f_M(z,t)$.

The current $I_S(z,t)$ and voltage $V_{\text{tot}}(z,t)$ of the series circuit are related as

$$V_{\text{tot}}(z,t) = R(z,t)I_S(z,t) + L(z,t)\frac{dI_S(z,t)}{dt} + I_S(z,t)\frac{dL(z,t)}{dt} + C_0^{-1}\int^t I_S(z,t')dt'. \tag{30}$$

Following the same mathematical treatment as in Sec. II, we obtain the coupling equation

$$\sum_{m=-\infty}^{+\infty} (R_0 + j\omega_n L_0)\, a_m i_{S,n-m} + \frac{1}{j\omega_n C_0} i_{S,n} = v_n, \tag{31}$$

where $i_{S,n}$ and v_n are the nth-harmonic components of I_S and V_{tot}, respectively. The voltage and current vectors are related by the impedance matrix, $\mathbf{Z}_S \cdot \vec{i}_S = \vec{v}$. $\mathbf{Z}_S$ is a $(2N+1)\times(2N+1)$ matrix filled with elements

$$Z_S(s,t) = (R_0 + j\omega_s L_0)\, a_{s-t} + \frac{\delta(s-t)}{j\omega_s C_0}, \tag{32}$$

where $\delta(x)$ is the Dirac δ function. After $\mathbf{Z}_S$ is known, the admittance matrix is found by inversion: $\mathbf{Y}_S = \mathbf{Z}_S^{-1}$. For a given grounded substrate, we can obtain its admittance matrix $\mathbf{Y}_G$ and further the total admittance $\mathbf{Y}_{\text{tot}}$, as explained in Sec. II. Finally, the scattering harmonics can be calculated from Eq. (14).

The above theory can be used for the design of wave isolators following the ideas presented in Sec. III A. With a proper modulation function applied on graphene array, the incident wave can be fully converted into evanescent modes for waves from $\theta = +\theta_i$, while for the opposite tilted angle it is mostly reflected in the specular direction. To find such a modulation function, we assume two unknown Fourier terms in Eq. (29), a_1 and a_2. For a fixed modulation frequency ($\omega_M = 200$ GHz) and incident angle ($\theta = +45°$), a set of a_1, a_2, and E_{F0} (which determines the static resistance and inductance) can be optimized to

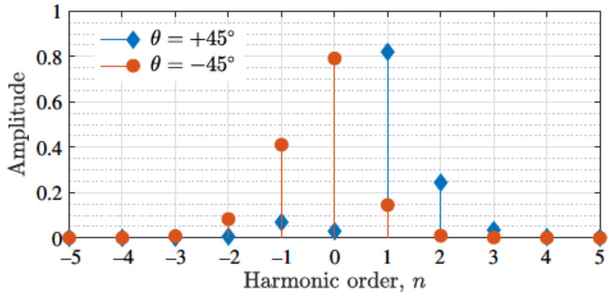

FIG. 12. Distribution of harmonics at $\omega_0 = 12$ THz for incidence angles $\theta = +45°$ and $\theta = -45°$. $\beta_M = 5.86 \times 10^5\ \mathrm{m}^{-1}$, $E_{F0} = 1.0$ eV, $\tau = 0.5$ ps, $a_1 = 0.138$, and $a_2 = 0$. The substrate is assumed to have $d = 4\ \mu$m and $\epsilon_r = 4$.

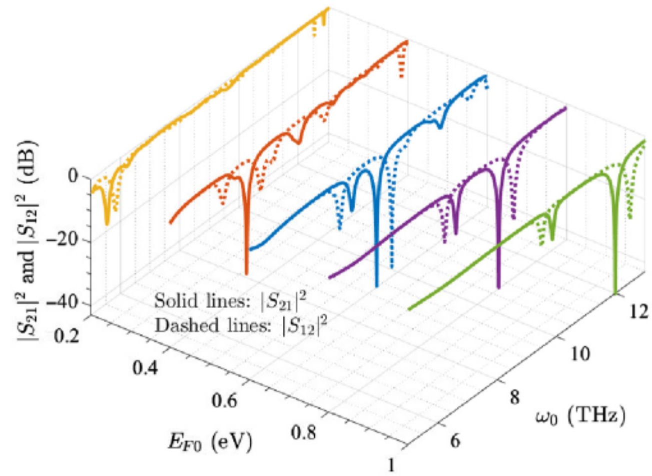

FIG. 13. Frequency spectrum of the device for incidences from $\theta = +45°$ (solid lines) and $\theta = -45°$ (dashed lines). Green lines correspond to $a_1 = 0.138$, $a_2 = 0$, and $E_{F0} = 1.0$ eV. Purple lines corrrespond to $a_1 = 0.165$, $a_2 = 0$, and $E_{F0} = 0.8$ eV. Blue lines correspond to $a_1 = 0.195$, $a_2 = 0$, and $E_{F0} = 0.6$ eV. Red lines correspond to $a_1 = 0.235$, $a_2 = 0$, and $E_{F0} = 0.4$ eV. Yellow lines correspond to $a_1 = 0.317$, $a_2 = 0.183$, and $E_{F0} = 0.2$ eV.

fully suppress the specular harmonic and convert the incident wave into evanescent modes. Fig. 12 shows that at $\omega_0 = 12$ THz, the wave incident from $\theta = +45°$ is indeed transformed into the first-order evanescent harmonic with a strong amplitude of $A_1 = 0.8$. Swapping the incident direction invalidates the phase-matching condition, and, as a consequence, the evanescent amplitudes become weak. Therefore, most of the incident energy is reflected via the specular channel.

At other frequencies we can always find an optimal set of a_1, a_2, and E_{F0} to reconstruct the isolation functionality. Figure 13 shows that the absorption frequency (from $\theta = +45°$) decreases as we lower the medium Fermi level of graphene E_{F0}. In addition, to achieve good isolation performance, the modulation function $f_M(z, t)$ should be reoptimized to maximize the absorption level. Because of the modifications of the modulation function, the isolator can operate over a wide band from 5.5 to 12 THz without sacrificing the isolation performance.

The isolation is determined by forward attenuation as well as by reversed insertion loss. After perfect absorption is ensured in the forward direction ($S_{21} = 0$), the transmission for the opposite incidence S_{12} is affected by the modulation speed as well as the resonance strength of the system, which determine the spectral distance between the two transmission minima. The resonance of the structure can be enhanced by use of low-resistivity (high-mobility) graphene. Simultaneously, reducing the resistance of graphene also helps to relax limitations on the modulation speed since the maximum modulation frequency is determined by the intrinsic RC time constant of graphene capacitors ($\omega_M^{\max} = 1/RC$, where R and C are the effective resistance and capacitance of the graphene gating) [61]. Theoretical estimations have shown that with high-quality graphene layers, the modulation speed can reach several hundred gigahertz [62,63]. However, in standard fabrication technology, graphene mobility significantly decreases during the fabrication process due to unavoidable impurities and contamination from the environment [[64], §1.3]. In consequence, with conventional graphene fabrication techniques, it is still a challenge to reach the modulation speed assumed in this example. On the other hand, recent advances have shown that with use of an atomically flat substrate (e.g., hexagonal BN) [65], postannealing, and improved transfer techniques [66], it is possible to obtain high-quality graphene. In addition, the present electrical modulation might be replaced by an optical modulation scheme with significantly increased modulation speed [67,68].

V. CONCLUSIONS

In this paper, we introduce a general approach to realize nonreciprocal metasurface devices to control waves in single or multiple scattering channels in free space. Importantly, we show that a variety of functionalities can be realized with the same physical platform by adjusting the space-time modulation of the single tunable element: an impedance sheet. As examples, the proposed technique is applied to design nonreciprocal metasurfaces that act as isolators, nonreciprocal phase shifters, quasi-isolators, and circulators. In addition, a graphene-based modulation platform is proposed, where the isolation frequency can be dynamically tuned over a wide frequency range by changing the modulation function. We expect that the technique introduced here will be useful in the developments of future computer-controlled intelligent nonreciprocal metasufaces for various applications.

ACKNOWLEDGMENTS

This work received funding from the Foundation for Aalto University Science and Technology, the Academy of Finland (project 309421), the European Union Horizon 2020 research and innovation program—Future Emerging Technologies (FET Open)—under Grant Agreement No. 736876, and the U.S. Air Force Office of Scientific Research. The authors thank Dr. Viktar Asadchy, Dr. Dimitrios Sounas, Dr. Fu Liu, and Dr. Beibei Kong for helpful discussions.

[1] V. Asadchy, A. Díaz-Rubio, S. Tcvetkova, D.-H. Kwon, A. Elsakka, M. Albooyeh, and S. Tretyakov, Flat Engineered Multichannel Reflectors, Phys. Rev. X 7, 031046 (2017).

[2] X. Wang, A. Díaz-Rubio, V. S. Asadchy, G. Ptitcyn, A. A. Generalov, J. Ala-Laurinaho, and S. A. Tretyakov, Extreme Asymmetry in Metasurfaces via Evanescent Fields Engineering: Angular-Asymmetric Absorption, Phys. Rev. Lett. **121**, 256802 (2018).

[3] A. Díaz-Rubio, V. S. Asadchy, A. Elsakka, and S. A. Tretyakov, From the generalized reflection law to the realization of perfect anomalous reflectors, Sci. Adv. **3**, e1602714 (2017).

[4] V. S. Asadchy, M. Albooyeh, S. N. Tcvetkova, A. Díaz-Rubio, Y. Radi, and S. Tretyakov, Perfect control of reflection and refraction using spatially dispersive metasurfaces, Phys. Rev. B **94**, 075142 (2016).

[5] Y. Radi, D. L. Sounas, and A. Alù, Metagratings: Beyond the Limits of Graded Metasurfaces for Wave Front Control, Phys. Rev. Lett. **119**, 067404 (2017).

[6] F. Liu, O. Tsilipakos, A. Pitilakis, A. C. Tasolamprou, M. S. Mirmoosa, N. V. Kantartzis, D.-H. Kwon, M. Kafesaki, C. M. Soukoulis, and S. A. Tretyakov, Intelligent Metasurfaces with Continuously Tunable Local Surface Impedance for Multiple Reconfigurable Functions, Phys. Rev. Appl. **11**, 044024 (2019).

[7] J. D. Adam, L. E. Davis, G. F. Dionne, E. F. Schloemann, and S. N. Stitzer, Ferrite devices and materials, IEEE Trans. Microw. Theory Tech. **50**, 721 (2002).

[8] M. Tamagnone, C. Moldovan, J.-M. Poumirol, A. B. Kuzmenko, A. M. Ionescu, J. R. Mosig, and J. Perruisseau-Carrier, Near optimal graphene terahertz non-reciprocal isolator, Nat. Commun. **7**, 11216 (2016).

[9] I. Crassee, J. Levallois, A. L. Walter, M. Ostler, A. Bostwick, E. Rotenberg, T. Seyller, D. Van Der Marel, and A. B. Kuzmenko, Giant faraday rotation in single-and multilayer graphene, Nat. Phys. **7**, 48 (2011).

[10] D. L. Sounas and C. Caloz, Gyrotropy and nonreciprocity of graphene for microwave applications, IEEE Trans. Microw. Theory Tech. **60**, 901 (2012).

[11] D. L. Sounas, J. Soric, and A. Alù, Broadband passive isolators based on coupled nonlinear resonances, Nat. Electron. **1**, 113 (2018).

[12] A. M. Mahmoud, A. R. Davoyan, and N. Engheta, All-passive nonreciprocal metastructure, Nat. Commun. **6**, 8359 (2015).

[13] G. D'Aguanno, D. L. Sounas, H. M. Saied, and A. Alù, Nonlinearity-based circulator, Appl. Phys. Lett. **114**, 181102 (2019).

[14] Y. Shi, Z. Yu, and S. Fan, Limitations of nonlinear optical isolators due to dynamic reciprocity, Nat. Photonics **9**, 388 (2015).

[15] D. L. Sounas and A. Alù, Fundamental bounds on the operation of fano nonlinear isolators, Phys. Rev. B **97**, 115431 (2018).

[16] G. Ptitcyn, M. Mirmoosa, and S. Tretyakov, Time-modulated meta-atoms, Phys. Rev. Res. **1**, 023014 (2019).

[17] M. Mirmoosa, G. Ptitcyn, V. Asadchy, and S. Tretyakov, Time-Varying Reactive Elements for Extreme Accumulation of Electromagnetic Energy, Phys. Rev. Appl. **11**, 014024 (2019).

[18] D. L. Sounas and A. Alù, Non-reciprocal photonics based on time modulation, Nat. Photonics **11**, 774 (2017).

[19] L. Yuan and S. Fan, Three-Dimensional Dynamic Localization of Light from a Time-Dependent Effective Gauge Field for Photons, Phys. Rev. Lett. **114**, 243901 (2015).

[20] S. Buddhiraju, W. Li, and S. Fan, Photonic Refrigeration from Time-Modulated Thermal Emission, Phys. Rev. Lett. **124**, 077402 (2020).

[21] T. T. Koutserimpas and R. Fleury, Nonreciprocal Gain in Non-Hermitian Time-Floquet Systems, Phys. Rev. Lett. **120**, 087401 (2018).

[22] M. Liu, D. A. Powell, Y. Zarate, and I. V. Shadrivov, Huygens Metadevices for Parametric Waves, Phys. Rev. X **8**, 031077 (2018).

[23] A. Mock, D. Sounas, and A. Alù, Magnet-free circulator based on spatiotemporal modulation of photonic crystal defect cavities, ACS Photonics **6**, 2056 (2019).

[24] Y. Hadad, J. C. Soric, and A. Alù, Breaking temporal symmetries for emission and absorption, Proc. Natl. Acad. Sci. U. S. A. **113**, 3471 (2016).

[25] S. Taravati and A. A. Kishk, Space-time modulation: Principles and applications, IEEE Microw. Mag. **21**, 30 (2020).

[26] A. M. Shaltout, V. M. Shalaev, and M. L. Brongersma, Spatiotemporal light control with active metasurfaces, Science **364**, eaat3100 (2019).

[27] Z. Yu and S. Fan, Complete optical isolation created by indirect interband photonic transitions, Nat. Photonics **3**, 91 (2009).

[28] H. Lira, Z. Yu, S. Fan, and M. Lipson, Electrically Driven Nonreciprocity Induced by Interband Photonic Transition on a Silicon Chip, Phys. Rev. Lett. **109**, 033901 (2012).

[29] Z. Yu and S. Fan, Integrated nonmagnetic optical isolators based on photonic transitions, IEEE J. Sel. Top. Quant. Electron. **16**, 459 (2009).

[30] D. Correas-Serrano, A. Alù, and J. Gomez-Diaz, Magnetic-free nonreciprocal photonic platform based on time-modulated graphene capacitors, Phys. Rev. B **98**, 165428 (2018).

[31] C. Qin, B. Wang, H. Long, K. Wang, and P. Lu, Nonreciprocal phase shift and mode modulation in dynamic graphene waveguides, J. Lightwave Technol. **34**, 3877 (2016).

[32] N. Chamanara, S. Taravati, Z.-L. Deck-Léger, and C. Caloz, Optical isolation based on space-time engineered

asymmetric photonic band gaps, Phys. Rev. B **96**, 155409 (2017).
[33] S. Taravati, N. Chamanara, and C. Caloz, Nonreciprocal electromagnetic scattering from a periodically space-time modulated slab and application to a quasisonic isolator, Phys. Rev. B **96**, 165144 (2017).
[34] S. Taravati, Self-biased broadband magnet-free linear isolator based on one-way space-time coherency, Phys. Rev. B **96**, 235150 (2017).
[35] Y. Hadad, D. Sounas, and A. Alù, Space-time gradient metasurfaces, Phys. Rev. B **92**, 100304 (2015).
[36] Y. Shi, S. Han, and S. Fan, Optical circulation and isolation based on indirect photonic transitions of guided resonance modes, ACS Photonics **4**, 1639 (2017).
[37] N. A. Estep, D. L. Sounas, and A. Alù, Magnetless microwave circulators based on spatiotemporally modulated rings of coupled resonators, IEEE Trans. Microw. Theory Tech. **64**, 502 (2016).
[38] S. Taravati and A. A. Kishk, Dynamic modulation yields one-way beam splitting, Phys. Rev. B **99**, 075101 (2019).
[39] M. M. Salary, S. Jafar-Zanjani, and H. Mosallaei, Time-varying metamaterials based on graphene-wrapped microwires: Modeling and potential applications, Phys. Rev. B **97**, 115421 (2018).
[40] M. M. Salary, S. Jafar-Zanjani, and H. Mosallaei, Electrically tunable harmonics in time-modulated metasurfaces for wavefront engineering, New J. Phys. **20**, 123023 (2018).
[41] Y. Hadad and D. Sounas, Space-time modulated loaded-wire metagratings for magnetless nonreciprocity and near-complete frequency conversion. Preprint arXiv:1906.00215, 2019.
[42] S. Taravati and C. Caloz, Mixer-duplexer-antenna leaky-wave system based on periodic space-time modulation, IEEE T. Antenn. Propag. **65**, 442 (2017).
[43] D. Correas-Serrano, J. Gomez-Diaz, D. Sounas, Y. Hadad, A. Alvarez-Melcon, and A. Alù, Nonreciprocal graphene devices and antennas based on spatiotemporal modulation, IEEE Antenn. Wirel. Pr. **15**, 1529 (2016).
[44] J. Zang, D. Correas-Serrano, J. Do, X. Liu, A. Alvarez-Melcon, and J. Gomez-Diaz, Nonreciprocal Wavefront Engineering with Time-Modulated Gradient Metasurfaces, Phys. Rev. Appl. **11**, 054054 (2019).
[45] See Supplemental Material at http://link.aps.org/supplemental/10.1103/PhysRevApplied.13.044040 for additional information on derivation of Eq. 1, derivation of the harmonic frequency and wave number, derivation of the admittance matrix of space-time-modulated inductance, derivation of Eq. 11, derivation of the diffraction limit, and the optimization code.
[46] S. Y. Elnaggar and G. N. Milford, Generalized space-time periodic circuits for arbitrary structures. preprint arXiv:1901.08698, 2019.
[47] D. M. Pozar, *Microwave Engineering* (John Wiley & Sons, Hoboken, New Jersey, 2009).
[48] A. Shaltout, A. Kildishev, and V. Shalaev, Time-varying metasurfaces and lorentz non-reciprocity, Opt. Mater. Express **5**, 2459 (2015).
[49] F. Yang and Y. Rahmat-Samii, eds., *Surface Electromagnetics: With Applications in Antenna, Microwave, and Optical Engineering* (Cambridge University Press, Cambridge, 2019).
[50] X. Wang, A. Díaz-Rubio, A. Sneck, A. Alastalo, T. Mäkelä, J. Ala-Laurinaho, J.-F. Zheng, A. V. Räisänen, and S. A. Tretyakov, Systematic design of printable metasurfaces: Validation through reverse-offset printed millimeter-wave absorbers, IEEE T. Antenn. Propag. **66**, 1340 (2018).
[51] A. Li, S. Singh, and D. Sievenpiper, Metasurfaces and their applications, Nanophotonics **7**, 989 (2018).
[52] D. Chicherin, S. Dudorov, D. Lioubtchenko, V. Ovchinnikov, S. Tretyakov, and A. V. Räisänen, Mems-based high-impedance surfaces for millimeter and submillimeter wave applications, Microw. Opt. Technol. Lett. **48**, 2570 (2006).
[53] D. F. Sievenpiper, J. H. Schaffner, H. J. Song, R. Y. Loo, and G. Tangonan, Two-dimensional beam steering using an electrically tunable impedance surface, IEEE T. Antenn. Propag. **51**, 2713 (2003).
[54] D. Sievenpiper and J. Schaffner, Beam steering microwave reflector based on electrically tunable impedance surface, Electron. Lett. **38**, 1237 (2002).
[55] F. Liu, O. Tsilipakos, X. Wang, A. Pitilakis, A. C. Tasolamprou, M. S. Mirmoosa, D.-H. Kwon, K. Kossifos, J. Georgiou, M. Kafesaki *et al.*, in *2018 12th International Congress on Artificial Materials for Novel Wave Phenomena (Metamaterials)* (IEEE, 2019) pp. 260–262.
[56] A. Pitilakis, A. C. Tasolamprou, C. Liaskos, F. Liu, O. Tsilipakos, X. Wang, M. S. Mirmoosa, K. Kossifos, J. Georgiou, A. Pitsilides *et al.*, in *2018 12th International Congress on Artificial Materials for Novel Wave Phenomena (Metamaterials)* (IEEE, 2018) pp. 483–485.
[57] A. C. Tasolamprou, A. Pitilakis, S. Abadal, O. Tsilipakos, X. Timoneda, H. Taghvaee, M. S. Mirmoosa, F. Liu, C. Liaskos, A. Tsioliaridou *et al.*, Exploration of intercell wireless millimeter-wave communication in the landscape of intelligent metasurfaces, IEEE Access **7**, 122931 (2019).
[58] L. Petrou, P. Karousios, and J. Georgiou, in *2018 IEEE International Symposium on Circuits and Systems (ISCAS)* (IEEE, 2018) pp. 1–5.
[59] O. Luukkonen, C. Simovski, G. Granet, G. Goussetis, D. Lioubtchenko, A. V. Raisanen, and S. A. Tretyakov, Simple and accurate analytical model of planar grids and high-impedance surfaces comprising metal strips or patches, IEEE T. Antenn. Propag. **56**, 1624 (2008).
[60] S. Tretyakov and C. Simovski, Dynamic model of artificial reactive impedance surfaces, J. Electromagnet. Wave Appl. **17**, 131 (2003).
[61] Z. Sun, A. Martinez, and F. Wang, Optical modulators with 2d layered materials, Nat. Photonics **10**, 227 (2016).
[62] J. Gosciniak and D. T. Tan, Theoretical investigation of graphene-based photonic modulators, Sci. Rep. **3**, 1 (2013).
[63] S. J. Koester and M. Li, High-speed waveguide-coupled graphene-on-graphene optical modulators, Appl. Phys. Lett. **100**, 171107 (2012).
[64] L. Wang, Ph.D. thesis, Columbia University, 2014.

[65] C. R. Dean, A. F. Young, I. Meric, C. Lee, L. Wang, S. Sorgenfrei, K. Watanabe, T. Taniguchi, P. Kim, K. L. Shepard *et al.*, Boron nitride substrates for high-quality graphene electronics, Nat. Nanotechnol. **5**, 722 (2010).

[66] L. Banszerus, M. Schmitz, S. Engels, J. Dauber, M. Oellers, F. Haupt, K. Watanabe, T. Taniguchi, B. Beschoten, and C. Stampfer, Ultrahigh-mobility graphene devices from chemical vapor deposition on reusable copper, Sci. Adv. **1**, e1500222 (2015).

[67] W. Li, B. Chen, C. Meng, W. Fang, Y. Xiao, X. Li, Z. Hu, Y. Xu, L. Tong, H. Wang *et al.*, Ultrafast all-optical graphene modulator, Nano Lett. **14**, 955 (2014).

[68] R. Duggan, D. Sounas, and A. Alù, Optically driven effective faraday effect in instantaneous nonlinear media, Optica **6**, 1152 (2019).